Modeling, Analysis and Testing of Autonomous Operation of an Inverter-Based Microgrid

Nagaraju Pogaku, *Student Member, IEEE*, Milan Prodanović, *Member, IEEE*, and
Timothy C. Green, *Senior Member, IEEE*

Abstract—The analysis of the small-signal stability of conventional power systems is well established, but for inverter based microgrids there is a need to establish how circuit and control features give rise to particular oscillatory modes and which of these have poor damping. This paper develops the modeling and analysis of autonomous operation of inverter-based microgrids. Each sub-module is modeled in state-space form and all are combined together on a common reference frame. The model captures the detail of the control loops of the inverter but not the switching action. Some inverter modes are found at relatively high frequency and so a full dynamic model of the network (rather than an algebraic impedance model) is used. The complete model is linearized around an operating point and the resulting system matrix is used to derive the eigenvalues. The eigenvalues (termed "modes") indicate the frequency and damping of oscillatory components in the transient response. A sensitivity analysis is also presented which helps identifying the origin of each of the modes and identify possible feedback signals for design of controllers to improve the system stability. With experience it is possible to simplify the model (reduce the order) if particular modes are not of interest as is the case with synchronous machine models. Experimental results from a microgrid of three 10-kW inverters are used to verify the results obtained from the model.

Index Terms—Inverter, inverter model, microgrid, power control, small-signal stability.

I. INTRODUCTION

RECENT innovations in small-scale distributed power generation systems combined with technological advancements in power electronic systems led to concepts of future network technologies such as microgrids. These small autonomous regions of power systems can offer increased reliability and efficiency and can help integrate renewable energy and other forms of distributed generation (DG) [1]. Many forms of distributed generation such as fuel-cells, photo-voltaic and micro-turbines are interfaced to the network through power electronic converters [2]–[5]. These interface devices make the sources more flexible in their operation and control compared to the conventional electrical machines. However, due to their

negligible physical inertia they also make the system potentially susceptible to oscillation resulting from network disturbances.

A microgrid can be operated either in grid connected mode or in stand-alone mode. In grid connected mode, most of the system-level dynamics are dictated by the main grid due to the relatively small size of micro sources. In stand-alone mode, the system dynamics are dictated by micro sources themselves, their power regulation control and, to an unusual degree, by the network itself.

One of the important concerns in the reliable operation of a microgrid is small-signal stability. In conventional power systems, stability analysis is well established and for the different frequency ranges (or time horizons) of possible concern there are models which include the appropriate features. The features have been established on the basis of decades of experience so that there are standard models of synchronous machines, governors and excitation systems of varying orders that are known to capture the important modes for particular classes of problem. This does not yet exist for microgrids and may be difficult to achieve because of the range of power technologies that might be deployed. However, we can begin by developing full-order models of inverters and the inverter equivalents of governors and exciters. Examination of these models applied to various systems will develop that body of experience that allows reduced order models to be selected for some problems.

Previous dynamic analysis of standalone systems has been carried out by assuming an ideal inverter as in [6]. This means that the closed-loop inner controllers that track voltage and current references are assumed to track perfectly, accurately and quickly. They therefore do not have any effect on the small signal stability. This assumption is based on the fact that the closed-loop bandwidth of the inverter is well above the bandwidth of power sharing controllers that set the voltage and current references. This is a relatively safe assumption for low power inverters with a high switching frequency but cause important dynamics to be omitted for large inverters where low switching frequency limits the control bandwidth of the innermost control loop. The modeling approach presented in [7] concentrates on stability issues for an individual inverter connected to a stiff ac bus. This is valuable in illuminating inverter properties but needs extension to cover the interaction of inverters with each other and with network dynamics before it can indicate the nature of stability issues in microgrids.

In this paper, a systematic approach to modeling an inverter-based microgrid is presented. Each DG inverter will have an outer power loop based on droop control to share the fundamental real and reactive powers with other DGs. Inverter internal controls will include voltage and current controllers

which are designed to reject high frequency disturbances and damp the output LC filter to avoid any resonance with the external network. The small-signal state-space model of an individual inverter is constructed by including the controllers, output filter and coupling inductor on a synchronous reference frame whose rotation frequency is set by the power controller of that inverter. An arbitrary choice is made to select one inverter frame as the common reference frame and all other inverters are translated to this common reference frame using the simple transformation techniques familiar in synchronous machine systems. It is considered that state-less impedance models of the network are inadequate for use with full-order inverter models which include high frequency modes. Instead a dynamic (state-space) model of the network is formed on the common reference frame.

Once the small-signal model has been formed, eigenvalues (or modes) are identified that indicate the frequency and damping of the oscillatory terms of the system transient response. The analytical nature of this examination then allows further investigation so that the relation between system stability and system parameters, such as the gains of controllers, is established. A sensitivity analysis is then conducted which provides the sensitivity of different modes to the system state variables and points out the role of each controller in forming of these modes. States associated with modes that are not of interest in a particular problem can then be considered for removal from the model in order to simplify the analysis. This represents a systematic approach to finding appropriate models and avoids the danger of neglecting a system feature that later turns out to be important.

II. MICROGRID MODEL IN AUTONOMOUS OPERATION

A typical characteristic of a microgrid is that it can be operated either in grid connected or in islanded (autonomous) mode. Normally, when a microgrid is operated in grid connected mode the micro sources act as constant power sources which means that they are controlled to inject the demanded power in to the network. In autonomous mode the micro sources are controlled to supply all the power needed by the local loads while maintaining the voltage and frequency within the allowed limits. Autonomous operation of a microgrid might be initiated for either of the following two reasons. First, because of preplanned (intentional) islanding due to maintenance or economical reasons. Depending on the market situation the owner of a microgrid can chose between autonomous and grid connected modes [8]. Second, because of unplanned (unintentional) islanding due to the failure of the main grid caused by a network fault.

Autonomous operation is realized by opening the isolating switch (shown in Fig. 1) which disconnects the microgrid from the main grid. Once the microgrid is isolated the micro sources feeding the system are responsible for maintaining the voltage and frequency while sharing the power. During autonomous operation it is important to avoid over-loading of inverters and to ensure that the changes in load are taken by inverters in a well controlled manner. Control techniques based on a communication link, such as the master-slave approach [9], can be adapted in systems where micro sources are connected to a common bus or located in close proximity. However, a communication link makes the system more expensive and less reliable. Also, in a
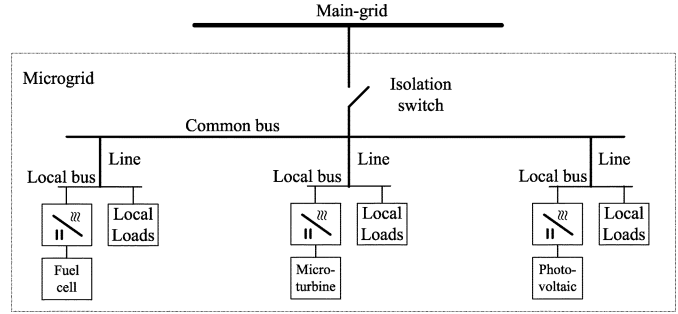

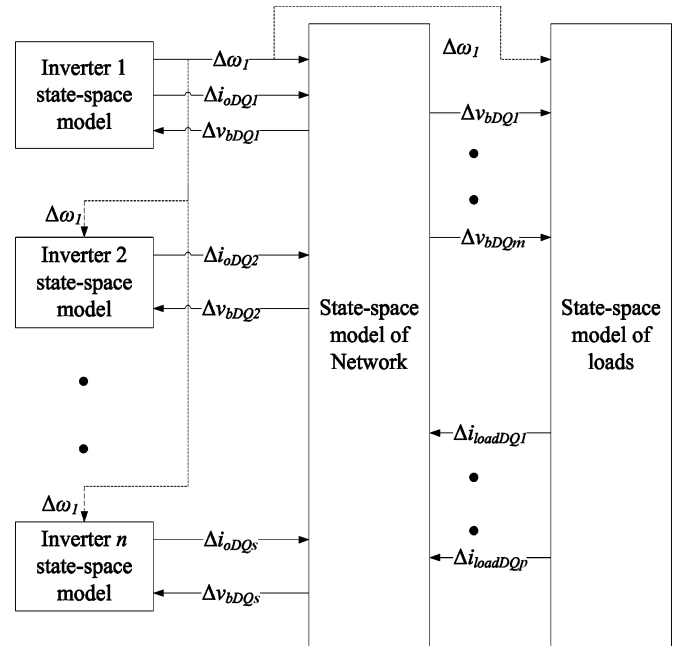Fig. 1. Typical structure of inverter-based microgrid.

Fig. 2. Block diagram of complete small-signal state-space model of a microgrid.

typical microgrid micro sources can be located far away from each other making a communication link less attractive. Control techniques based on local measurements which do not require expensive communication facilities have been proposed [10]. In this paper, the later method is adopted.

The modeling approach presented in this paper divides the whole system into three major sub-modules; inverter, network and loads (Fig. 2). Each inverter is modeled on its individual reference frame whose rotation frequency is set by its local power sharing controller. The inverter model includes the power sharing controller dynamics, output filter dynamics, coupling inductor dynamics and voltage and current controller dynamics. These last two element introduce high frequency dynamics which are apparent at peak and light load conditions and during large changes in load. The small-signal flow among the sub-modules shown in Fig. 2 will be explained in the following sections.

Network dynamics are generally neglected in small-signal modeling of conventional power systems. The reason behind this is that the time constants of rotating machines and their controls are much larger than those of the network. In the case of microgrids, the micro sources are connected through
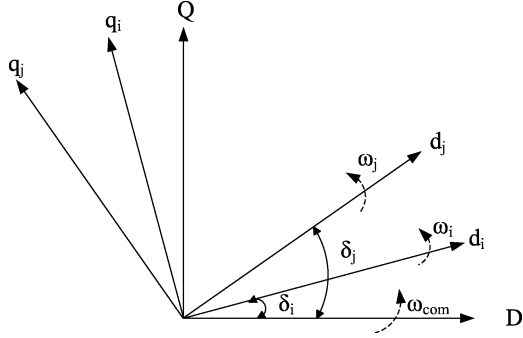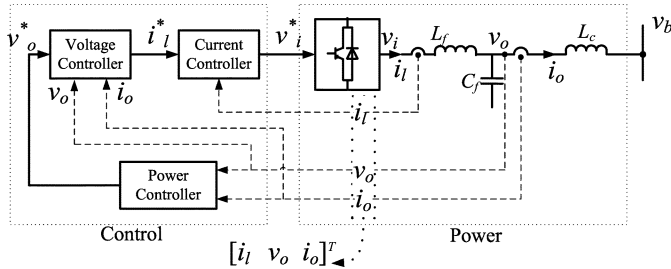
Fig. 3. Reference frame transformation.

Fig. 4. DG inverter block diagram.

Fig. 5. Power controller.

inverters whose response times are very small and network dynamics would influence the system stability. Previous work [6] on small-signal modeling of parallel connected inverters was carried out without considering the network dynamics.

Here, the state equations of the network and the loads are represented on the reference frame of one of the individual inverters. This reference frame is considered as the common reference frame. All the other inverters are translated to this common reference frame using the transformation technique [11] depicted in Fig. 3 and defined in (1). Here, the axis set $(D - Q)$ is the common reference frame rotating at a frequency ω_{com}, whereas axes $(d - q)_i$ and $(d - q)_j$ are the reference frame of ith and jth inverters rotating at ω_i and ω_j, respectively

$$[f_{DQ}] = [T_i][f_{dq}] \tag{1}$$

$$[T_i] = \begin{bmatrix} cos(\delta_i) & -sin(\delta_i) \\ sin(\delta_i) & cos(\delta_i) \end{bmatrix}. \tag{2}$$

In (1) and (2), δ_i is the angle of the reference frame of ith inverter with respect to the common reference frame. In the following sections the internal modeling of all the three modules is discussed in more detail. It is to be noted that in the equations of the following sections the three phase voltages and currents are represented as vectors in d–q frame, where as the other variables such as real and reactive powers and angles are scalars.

A. State-Space Model of a Voltage Source Inverter

Voltage source inverter is commonly used to interface distributed generators to the network. Fig. 4 shows the block diagram of an inverter connected to the microgrid. The power processing section consists of a three-leg inverter, an output LC filter and coupling inductor. Assuming an ideal source from the
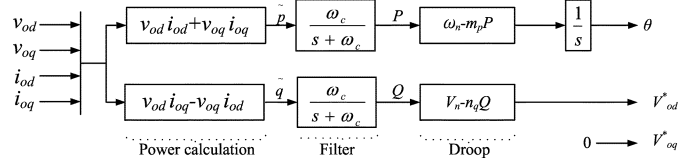
DG side, the dc bus dynamics can be neglected. With the realization of high switching frequencies (4–10 kHz), the switching process of the inverter may also be neglected.

The controller of a DG inverter can be divided into three different parts. First is an external power control loop which sets the magnitude and frequency (and hence phase) for the fundamental component of the inverter output voltage according to the droop characteristics set for the real and reactive powers (harmonic power sharing has been treated as an additional function with a different control topology [12]). The second and third parts of the control system are the voltage and current controllers, which are designed to reject high frequency disturbances and provide sufficient damping for the output LC filter [13], [14].

In this section, a state space model is presented for all of the subsystems: control loops, output filter and coupling inductor. The model is constructed in a rotational reference frame set by the external power controller of the particular individual inverter.

1) Power Controller: The basic idea behind the droop control is to mimic the governor of a synchronous generator. In a conventional power system, synchronous generators will share any increase in the load by decreasing the frequency according to their governor droop characteristic. This principle is implemented in inverters by decreasing the reference frequency when there is an increase in the load. Similarly, reactive power is shared by introducing a droop characteristic in the voltage magnitude.

As shown in Fig. 5, instantaneous active and reactive power components $\tilde{p}$ and $\tilde{q}$ are calculated from the measured output voltage and output current as in

$$\tilde{p} = v_{od}i_{od} + v_{oq}i_{oq}$$
$$\tilde{q} = v_{od}i_{oq} - v_{oq}i_{od}. \tag{3}$$

The instantaneous power components are passed through low-pass filters, shown in (4), to obtain the real and reactive powers P and Q corresponding to the fundamental component. ω_c represents the cut-off frequency of low-pass filters

$$P = \frac{\omega_c}{s + \omega_c}\tilde{p}, \quad Q = \frac{\omega_c}{s + \omega_c}\tilde{q}. \tag{4}$$

The real power sharing between inverters is obtained by introducing an artificial droop in the inverter frequency as in (5). The frequency ω is set according to the droop gain (m_p) and phase is set by integrating the frequency. This mimics to governor and inertia characteristics of conventional generators and provides a degree of negative feedback. For instance, if the power drawn from a generator increases then the rotation of its voltage slows and its angle retards. In the following equations ω_n will represent the nominal frequency set-point whereas α is the angle

of the inverter reference frame seen from a reference frame rotating at ω_n. From (5) it can be seen that the angle of the inverter voltage, α, changes in response to the real power flow in the required negative sense and with a gain set by the droop

$$\omega = \omega_n - m_p P$$

$$\dot{\theta} = \omega, \quad \theta = \omega_n t - \int m_p P dt$$

$$\alpha = -\int m_p P dt, \quad \dot{\alpha} = -m_p P. \tag{5}$$

To share the reactive power among multiple inverters, a droop is introduced in the voltage magnitude as given in (6). Here, V_n stands for the nominal set point of d-axis output voltage. The control strategy is chosen such that the output voltage magnitude reference is aligned to the d-axis of the inverter reference frame, and the q-axis reference is set to zero.

$$v_{od}^* = V_n - n_q Q, \quad v_{oq}^* = 0. \tag{6}$$

The droop gains m_p and n_q are calculated using (7) for the given range of frequency and voltage magnitude

$$m_p = \frac{\omega_{\max} - \omega_{\min}}{P_{\max}}, \quad n_q = \frac{V_{od\max} - V_{od\min}}{Q_{\max}}. \tag{7}$$

As discussed earlier, to construct the complete model on a common reference frame, the reference frame of one of the inverters is taken as the common frame. To translate the variables from an individual inverter reference frame onto the common frame, we define an angle δ for each inverter, given in (8). It should be noted that δ represents the angle between an individual inverter reference frame and the common reference frame, as shown in Fig. 3

$$\delta = \int (\omega - \omega_{\text{com}}). \tag{8}$$

Now, to allow a simpler system representation, the d and q axis components of voltages and currents in the following equations are combined to form vectors as in (9)

$$v_{odq}^* = [v_{od}^* \quad v_{oq}^*]^T, \quad i_{ldq} = [i_{ld} \quad i_{lq}]^T,$$

$$v_{odq} = [v_{od} \quad v_{oq}]^T, \quad i_{odq} = [i_{od} \quad i_{oq}]^T. \tag{9}$$

By linearizing and rearranging the equations above, the small-signal power controller model can be written in a state-space form as in (10). The outputs of the power controller are the small-signal variation of output voltage reference Δv_o^* and the frequency $\Delta\omega$. Matrices of (10) are defined in (11). An additional input signal $\Delta\omega_{\text{com}}$, which is the frequency deviation of the common reference frame, is also included in the model. It facilitates the connection of an individual inverter model to the common reference frame. This aspect is explained in Section (II-B)

$$\begin{bmatrix} \dot{\Delta\delta} \\ \dot{\Delta P} \\ \dot{\Delta Q} \end{bmatrix} = A_P \begin{bmatrix} \Delta\delta \\ \Delta P \\ \Delta Q \end{bmatrix} + B_P \begin{bmatrix} \Delta i_{ldq} \\ \Delta v_{odq} \\ \Delta i_{odq} \end{bmatrix} + B_{P\omega com}[\Delta\omega_{com}]$$

$$\begin{bmatrix} \Delta\omega \\ \Delta v_{odq}^* \end{bmatrix} = \begin{bmatrix} C_{P\omega} \\ C_{Pv} \end{bmatrix} \begin{bmatrix} \Delta\delta \\ \Delta P \\ \Delta Q \end{bmatrix} \tag{10}$$
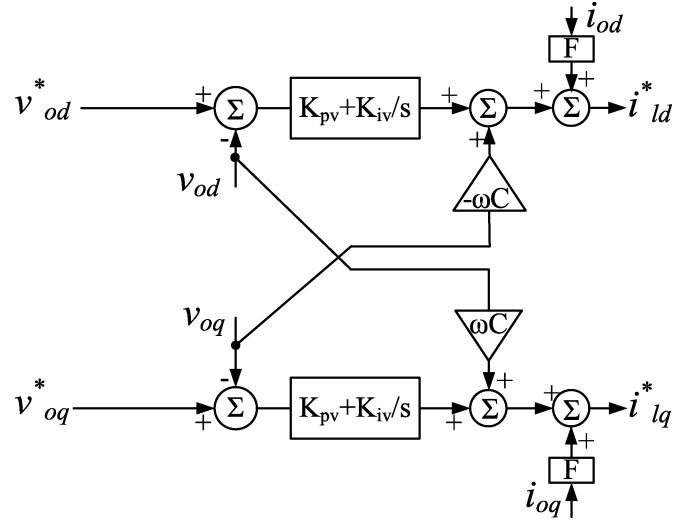

Fig. 6. Voltage controller.

$$A_P = \begin{bmatrix} 0 & -m_p & 0 \\ 0 & -\omega_c & 0 \\ 0 & 0 & -\omega_c \end{bmatrix} \quad B_{P\omega com} = \begin{bmatrix} -1 \\ 0 \\ 0 \end{bmatrix}$$

$$B_P = \begin{bmatrix} 0 & 0 & 0 & 0 & 0 & 0 \\ 0 & 0 & \omega_c I_{od} & \omega_c I_{oq} & \omega_c V_{od} & \omega_c V_{oq} \\ 0 & 0 & \omega_c I_{oq} & -\omega_c I_{od} & -\omega_c V_{oq} & \omega_c V_{od} \end{bmatrix}$$

$$C_{P\omega} = [0 \quad -m_p \quad 0] \quad C_{Pv} = \begin{bmatrix} 0 & 0 & -n_q \\ 0 & 0 & 0 \end{bmatrix}. \tag{11}$$

2) Voltage Controller: Fig. 6 shows the voltage controller block diagram including all feed-back and feed-forward terms. Output voltage control is achieved with a standard PI controller. The corresponding state equations are

$$\frac{d\phi_d}{dt} = v_{od}^* - v_{od}, \quad \frac{d\phi_q}{dt} = v_{oq}^* - v_{oq} \tag{12}$$

along with the algebraic equations

$$i_{ld}^* = F i_{od} - \omega_n C_f v_{oq} + K_{pv}(v_{od}^* - v_{od}) + K_{iv}\phi_d \tag{13}$$

$$i_{lq}^* = F i_{oq} + \omega_n C_f v_{od} + K_{pv}(v_{oq}^* - v_{oq}) + K_{iv}\phi_q. \tag{14}$$

Equations (15) and (18) represent the linearized small-signal state-space form of the voltage controller. Here, the input to the subsystem is split into two terms: the reference input and the feedback inputs

$$[\dot{\Delta\phi_{dq}}] = [0][\Delta\phi_{dq}] + B_{V1}[\Delta v_{odq}^*] + B_{V2} \begin{bmatrix} \Delta i_{ldq} \\ \Delta v_{odq} \\ \Delta i_{odq} \end{bmatrix}. \tag{15}$$

In (15)

$$\Delta\phi_{dq} = [\Delta\phi_d \quad \Delta\phi_q]^T \tag{16}$$

$$B_{V1} = \begin{bmatrix} 1 & 0 \\ 0 & 1 \end{bmatrix}, \quad B_{V2} = \begin{bmatrix} 0 & 0 & -1 & 0 & 0 & 0 \\ 0 & 0 & 0 & -1 & 0 & 0 \end{bmatrix} \tag{17}$$

$$[\Delta i_{ldq}^*] = C_V[\Delta\phi_{dq}] + D_{V1}[\Delta v_{odq}^*] + D_{V2} \begin{bmatrix} \Delta i_{ldq} \\ \Delta v_{odq} \\ \Delta i_{odq} \end{bmatrix} \tag{18}$$
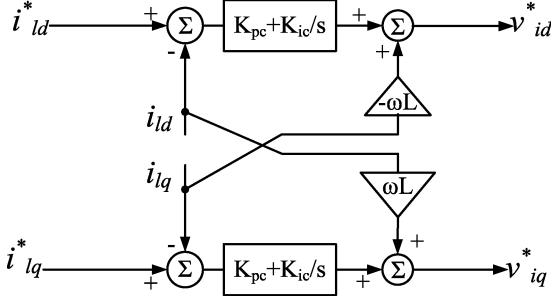
Fig. 7. Current controller.

$$C_V = \begin{bmatrix} K_{iv} & 0 \\ 0 & K_{iv} \end{bmatrix}, \quad D_{V1} = \begin{bmatrix} K_{pv} & 0 \\ 0 & K_{pv} \end{bmatrix}$$

$$D_{V2} = \begin{bmatrix} 0 & 0 & -K_{pv} & -\omega_n C_f & F & 0 \\ 0 & 0 & \omega_n C_f & -K_{pv} & 0 & F \end{bmatrix}. \quad (19)$$

3) Current Controller: Fig. 7 shows the current controller structure. Output filter inductor current control is achieved with a standard PI controller. The corresponding state equations are

$$\frac{d\gamma_d}{dt} = i_{ld}^* - i_{ld} \quad \frac{d\gamma_q}{dt} = i_{lq}^* - i_{lq} \quad (20)$$

along with the algebraic equations

$$v_{id}^* = -\omega_n L_f i_{lq} + K_{pc}\left(i_{ld}^* - i_{ld}\right) + K_{ic}\gamma_d \quad (21)$$

$$v_{iq}^* = \omega_n L_f i_{ld} + K_{pc}\left(i_{lq}^* - i_{lq}\right) + K_{ic}\gamma_q. \quad (22)$$

Equations (23) and (26) represent the linearized small-signal state-space form of current controller

$$[\Delta\dot{\gamma}_{dq}] = [0][\Delta\gamma_{dq}] + B_{C1}\left[\Delta i_{ldq}^*\right] + B_{C2}\begin{bmatrix} \Delta i_{ldq} \\ \Delta v_{odq} \\ \Delta i_{odq} \end{bmatrix} \quad (23)$$

where

$$\Delta\gamma_{dq} = [\Delta\gamma_d \quad \Delta\gamma_q]^T \quad (24)$$

$$B_{C1} = \begin{bmatrix} 1 & 0 \\ 0 & 1 \end{bmatrix}, \quad B_{C2} = \begin{bmatrix} -1 & 0 & 0 & 0 & 0 & 0 \\ 0 & -1 & 0 & 0 & 0 & 0 \end{bmatrix} \quad (25)$$

$$[\Delta v_{idq}^*] = C_C[\Delta\gamma_{dq}] + D_{C1}\left[\Delta i_{ldq}^*\right] + D_{C2}\begin{bmatrix} \Delta i_{ldq} \\ \Delta v_{odq} \\ \Delta i_{odq} \end{bmatrix} \quad (26)$$

$$C_C = \begin{bmatrix} K_{ic} & 0 \\ 0 & K_{ic} \end{bmatrix}, \quad D_{C1} = \begin{bmatrix} K_{pc} & 0 \\ 0 & K_{pc} \end{bmatrix}$$

$$D_{C2} = \begin{bmatrix} -K_{pc} & -\omega_n L_f & 0 & 0 & 0 & 0 \\ \omega_n L_f & -K_{pc} & 0 & 0 & 0 & 0 \end{bmatrix}. \quad (27)$$

4) Output LC Filter and Coupling Inductance: Output LC filter and the coupling inductance small-signal model can be represented with the following state equations by assuming that the inverter produces the demanded voltage ($v_i = v_i^*$):

$$\frac{di_{ld}}{dt} = \frac{-r_f}{L_f}i_{ld} + \omega i_{lq} + \frac{1}{L_f}v_{id} - \frac{1}{L_f}v_{od} \quad (28)$$

$$\frac{di_{lq}}{dt} = \frac{-r_f}{L_f}i_{lq} - \omega i_{ld} + \frac{1}{L_f}v_{iq} - \frac{1}{L_f}v_{oq} \quad (29)$$

$$\frac{dv_{od}}{dt} = \omega v_{oq} + \frac{1}{C_f}i_{ld} - \frac{1}{C_f}i_{od} \quad (30)$$

$$\frac{dv_{oq}}{dt} = -\omega v_{od} + \frac{1}{C_f}i_{lq} - \frac{1}{C_f}i_{oq} \quad (31)$$

$$\frac{di_{od}}{dt} = \frac{-r_c}{L_c}i_{od} + \omega i_{oq} + \frac{1}{L_c}v_{od} - \frac{1}{L_c}v_{bd} \quad (32)$$

$$\frac{di_{oq}}{dt} = \frac{-r_c}{L_c}i_{oq} - \omega i_{od} + \frac{1}{L_c}v_{oq} - \frac{1}{L_c}v_{bq}. \quad (33)$$

The following equations represent the linearized small-signal state-space form of the LC filter and coupling inductance. Frequency ω_0 is the system steady-state frequency at the given operating point

$$\begin{bmatrix} \Delta\dot{i}_{ldq} \\ \Delta v_{odq} \\ \Delta i_{odq} \end{bmatrix} = A_{LCL}\begin{bmatrix} \Delta i_{ldq} \\ \Delta v_{odq} \\ \Delta i_{odq} \end{bmatrix} + B_{LCL1}[\Delta v_{idq}]$$

$$+ B_{LCL2}[\Delta v_{bdq}] + B_{LCL3}[\Delta\omega] \quad (34)$$

$$A_{LCL} = \begin{bmatrix} \frac{-r_{L_f}}{L_f} & \omega_0 & \frac{-1}{L_f} & 0 & 0 & 0 \\ -\omega_0 & \frac{-r_{L_f}}{L_f} & 0 & \frac{-1}{L_f} & 0 & 0 \\ \frac{1}{C_f} & 0 & 0 & \omega_0 & -\frac{1}{C_f} & 0 \\ 0 & \frac{1}{C_f} & -\omega_0 & 0 & 0 & -\frac{1}{C_f} \\ 0 & 0 & \frac{1}{L_c} & 0 & \frac{-r_{L_c}}{L_c} & \omega_0 \\ 0 & 0 & 0 & \frac{1}{L_c} & -\omega_0 & \frac{-r_{L_c}}{L_c} \end{bmatrix}$$

$$B_{LCL1} = \begin{bmatrix} \frac{1}{L_f} & 0 \\ 0 & \frac{1}{L_f} \\ 0 & 0 \\ 0 & 0 \\ 0 & 0 \\ 0 & 0 \end{bmatrix} \quad B_{LCL2} = \begin{bmatrix} 0 & 0 \\ 0 & 0 \\ 0 & 0 \\ 0 & 0 \\ -\frac{1}{L_c} & 0 \\ 0 & -\frac{1}{L_c} \end{bmatrix}$$

$$B_{LCL3} = [I_{lq} \quad -I_{ld} \quad V_{oq} \quad -V_{od} \quad I_{oq} \quad -I_{od}]^T. \quad (35)$$

5) Complete Model of an Individual Inverter: To connect an inverter to the whole system the output variables need to be converted to the common reference frame. In this case the output variables of an inverter are the output currents represented as a vector Δi_{odq}. Using the transformation technique introduced in (1) and (2), the small-signal output current Δi_{oDQ} on the common reference frame can be obtained, as in (36). The small signal equivalent of the reference transformation is shown in Fig. 8

$$[\Delta i_{oDQ}] = [T_S][\Delta i_{odq}] + [T_C][\Delta\delta]. \quad (36)$$

where

$$T_S = \begin{bmatrix} cos(\delta_0) & -sin(\delta_0) \\ sin(\delta_0) & cos(\delta_0) \end{bmatrix}$$

$$T_C = \begin{bmatrix} -I_{od}sin(\delta_0) - I_{oq}cos(\delta_0) \\ I_{od}cos(\delta_0) - I_{oq}sin(\delta_0) \end{bmatrix}. \quad (37)$$

Similarly, the input signal to the inverter model is the bus voltage which is expressed on the common reference frame. The bus voltage can be converted to the individual inverter reference frame using reverse transformation, given by

$$[\Delta v_{bdq}] = \left[T_S^{-1}\right][\Delta v_{bDQ}] + \left[T_V^{-1}\right][\Delta\delta] \quad (38)$$

where

$$T_V^{-1} = \begin{bmatrix} -V_{bD}sin(\delta_0) + V_{bQ}cos(\delta_0) \\ -V_{bD}cos(\delta_0) - V_{bQ}sin(\delta_0) \end{bmatrix}. \quad (39)$$

It is to be noted that the inverter whose reference frame is taken as the common reference frame has to provide its reference frequency $\Delta\omega_{\text{com}}$ to all the sub-modules of the model as
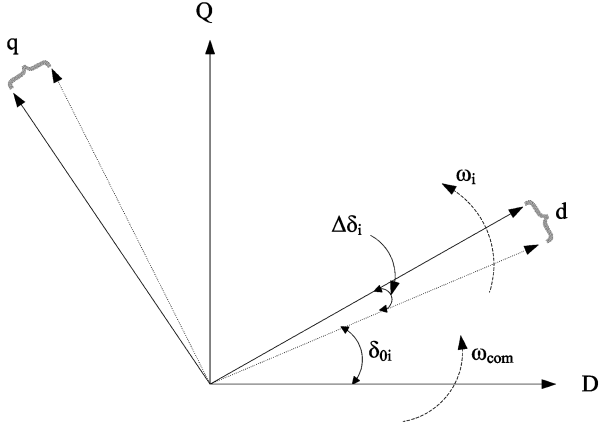
Fig. 8.   Small-signal equivalent of reference frame transformation.

shown in (8). Also, care should be taken to apply this modification in the power controller model shown in (10).

A complete state-space small-signal model of the inverter can be obtained by combining the state-space models of the power controller, voltage controller, current controller and output LCL filter, given by (10), (15), (18), (23), (26), (34), (36), and (38). There are totally 13 states, three inputs, and two outputs in each individual inverter model (except the inverter whose reference frame is the common reference frame, which has three outputs)

$$[\Delta \dot{x}_{\text{inv}i}] = A_{\text{INV}i}[\Delta x_{\text{inv}i}] + B_{\text{INV}i}[\Delta v_{bDQi}]$$
$$+ B_{i\omega com}[\Delta \omega_{\text{com}}] \tag{40}$$

$$\begin{bmatrix} \Delta \omega_i \\ \Delta i_{oDQi} \end{bmatrix} = \begin{bmatrix} C_{\text{INV}\omega i} \\ C_{\text{INV}ci} \end{bmatrix} [\Delta x_{\text{inv}i}]. \tag{41}$$

In (40) and (41)

$$\Delta x_{\text{inv}i} = [\Delta \delta_i \ \Delta P_i \ \Delta Q_i \ \Delta \phi_{dqi} \ \Delta \gamma_{dqi}$$
$$\Delta i_{ldqi} \ \Delta v_{odqi} \ \Delta i_{odqi}]^T \tag{42}$$

and (43)–(46), shown at the bottom of the page.

B. Combined Model of All the Inverters

In Section II-A5 the small-signal modelling of an individual DG inverter on a common reference frame was discussed. In a microgrid there can be several inverters acting as sources and connected remotely from each other. The modelling approach in this work is to form a sub-model of all the individual DG inverters and combine them with the network and individual load models.

Let us consider a system with "s" number of DG inverters where the reference frame of inverter number 1 is taken as the common reference frame. Then, from Section (II-A5), a combined small-signal model of all the inverter units together is obtained, as shown in

$$[\Delta \dot{x}_{\text{INV}}] = A_{\text{INV}}[\Delta x_{\text{INV}}] + B_{\text{INV}}[\Delta v_{bDQ}] \tag{47}$$
$$[\Delta i_{oDQ}] = C_{\text{INV}c}[\Delta x_{\text{INV}}]. \tag{48}$$

In (47) and (48)

$$[\Delta x_{\text{INV}}] = [\Delta x_{\text{inv}1} \ \Delta x_{\text{inv}2} \ \ldots \ \Delta x_{\text{inv } s}]^T \tag{49}$$

and (50)–(52), shown at the bottom of the next page.

C. Network Model

An example network of n lines and m nodes with s inverters and p load points is shown in Fig. 9. On a common reference frame the state equations of line current of ith line connected between nodes j and k are

$$\frac{di_{\text{lineD}i}}{dt} = \frac{-r_{\text{line}i}}{L_{\text{line}i}} i_{\text{lineD}i} + \omega i_{\text{lineQ}i}$$
$$+ \frac{1}{L_{\text{line}i}} v_{bDj} - \frac{1}{L_{\text{line}i}} v_{bDk} \tag{53}$$

$$\frac{di_{\text{lineQ}i}}{dt} = \frac{-r_{\text{line}i}}{L_{\text{line}i}} i_{\text{lineQ}i} - \omega i_{\text{lineD}i}$$
$$+ \frac{1}{L_{\text{line}i}} v_{bQj} - \frac{1}{L_{\text{line}i}} v_{bQk}. \tag{54}$$

$$A_{\text{INV}i} = \begin{bmatrix} A_{Pi} & 0 & 0 & B_{Pi} \\ B_{V1i}C_{Pvi} & 0 & 0 & B_{V2i} \\ B_{C1i}D_{V1i}C_{Pvi} & B_{C1i}C_{Vi} & 0 & B_{C1i}D_{V2i} + B_{C2i} \\ \begin{matrix} B_{LCL1i}D_{C1i}D_{V1i}C_{Pvi} + \\ B_{LCL2i}\begin{bmatrix} T_{Vi}^{-1} \ 0 \ 0 \end{bmatrix} + \\ B_{LCL3i}C_{P\omega i} \end{matrix} & B_{LCL1i}D_{C1i}C_{Vi} & B_{LCL1i}C_{Ci} & \begin{matrix} A_{LCLi} + \\ B_{LCL1i}(D_{C1i}D_{V2i} + D_{C2i}) \end{matrix} \end{bmatrix}_{13 \times 13} \tag{43}$$

$$B_{\text{INV}i} = \begin{bmatrix} 0 \\ 0 \\ 0 \\ B_{LCL2i}T_S^{-1} \end{bmatrix}_{13 \times 2} \quad B_{i\omega com} = \begin{bmatrix} B_{P\omega com} \\ 0 \\ 0 \\ 0 \end{bmatrix}_{13 \times 1} \tag{44}$$

$$C_{\text{INV}\omega i} = \begin{cases} [C_{P\omega} \ 0 \ 0 \ 0]_{1 \times 13} & i = 1 \\ [0 \ 0 \ 0 \ 0]_{1 \times 13} & i \neq 1 \end{cases} \tag{45}$$

$$C_{\text{INV}ci} = [[T_C \ 0 \ 0] \ 0 \ 0 \ [0 \ 0 \ T_S]]_{2 \times 13} \tag{46}$$
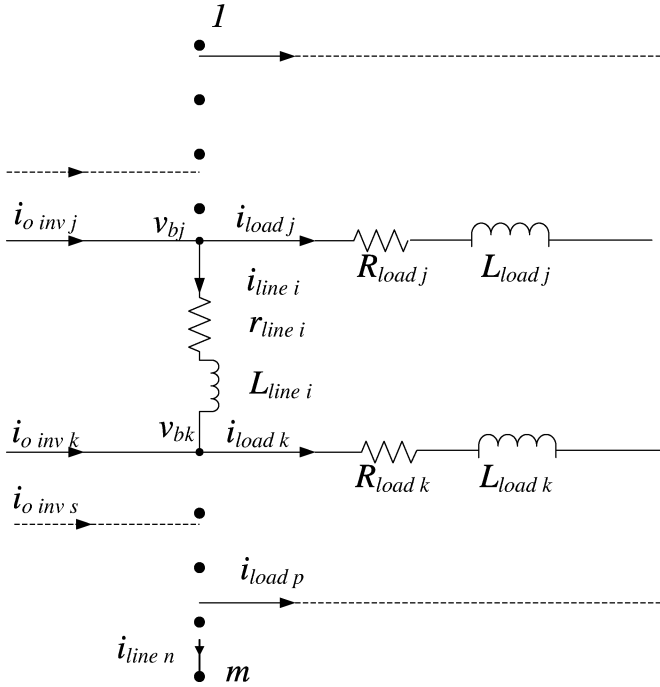
Fig. 9. Network representation.

Hence, the small-signal state-space model of a network with n lines is given by

$$[\Delta \dot{i}_{\text{lineDQ}}] = A_{\text{NET}}[\Delta i_{\text{lineDQ}}]$$
$$+ B_{1NET}[\Delta v_{bDQ}] + B_{2NET}\Delta\omega. \quad (55)$$

In (55)

$$[\Delta i_{\text{lineDQ}}] = [\Delta i_{\text{lineDQ 1}} \; \Delta i_{\text{lineDQ 2}}$$
$$\ldots \; \Delta i_{\text{lineDQ }n}]^T \quad (56)$$

$$[\Delta v_{bDQ}] = [\Delta v_{bDQ 1} \; \Delta v_{bDQ 2} \; \ldots \; \Delta v_{bDQ m}]^T \quad (57)$$

$$\Delta\omega = \Delta\omega_{\text{com}} \quad (58)$$

$$A_{\text{NET}} = \begin{bmatrix} A_{\text{NET 1}} & 0 & \ldots & 0 \\ 0 & A_{\text{NET 2}} & \ldots & 0 \\ \ldots & \ldots & \ldots & \ldots \\ 0 & 0 & \ldots & A_{\text{NET }n} \end{bmatrix}_{2n \times 2n} \quad (59)$$

$$B_{1NET} = \begin{bmatrix} B_{1NET 1} \\ B_{1NET 2} \\ .. \\ .. \\ B_{1NET n} \end{bmatrix}_{2n \times (2m)}$$

$$B_{2NET} = \begin{bmatrix} B_{2NET 1} \\ B_{2NET 2} \\ .. \\ .. \\ B_{2NET n} \end{bmatrix}_{2n \times 1} \quad (60)$$

where you get (61), shown at the bottom of the page.

D. Load Model

Although, many types of load can exist in microgrids, a general RL load is considered in this paper. The state equations of the RL load connected at ith node are

$$\frac{di_{\text{loadDi}}}{dt} = \frac{-R_{\text{loadi}}}{L_{\text{loadi}}}i_{\text{loadDi}} + \omega i_{\text{loadQi}} + \frac{1}{L_{\text{loadi}}}v_{bDi} \quad (62)$$

$$A_{\text{INV}} = \begin{bmatrix} A_{\text{INV1}} + B_{1\omega com}C_{\text{INV}\omega 1} & 0 & 0 & . \\ 0 & A_{\text{INV2}} + B_{2\omega com}C_{\text{INV}\omega 1} & 0 & . \\ . & . & . & . \\ . & . & . & A_{\text{INVs}} + B_{s\omega com}C_{\text{INV}\omega 1} \end{bmatrix}_{13s \times 13s} \quad (50)$$

$$B_{\text{INV}} = \begin{bmatrix} B_{\text{INV1}} \\ B_{\text{INV2}} \\ . \\ . \\ B_{\text{INVs}} \end{bmatrix}_{13s \times 2m}$$

$$[\Delta v_{bDQ}] = [\Delta v_{bDQ1} \; \Delta v_{bDQ2} \; . \; . \; \Delta v_{bDQm}] \quad (51)$$

$$C_{\text{INVc}} = \begin{bmatrix} [C_{\text{INVc1}}] & 0 & 0 & . \\ 0 & [C_{\text{INVc2}}] & 0 & . \\ . & . & . & . \\ . & . & . & [C_{\text{INVcs}}] \end{bmatrix}_{2s \times 13s} \quad (52)$$

$$A_{\text{NETi}} = \begin{bmatrix} \frac{-r_{\text{linei}}}{L_{\text{linei}}} & \omega_0 \\ -\omega_0 & \frac{-r_{\text{linei}}}{L_{\text{linei}}} \end{bmatrix} \quad B_{2NETi} = \begin{bmatrix} I_{\text{lineQi}} \\ -I_{\text{lineDi}} \end{bmatrix}$$

$$B_{1NETi} = \begin{bmatrix} \ldots & \frac{1}{L_{\text{linei}}} & 0 & \ldots & \frac{-1}{L_{\text{linei}}} & 0 & \ldots \\ \ldots & 0 & \frac{1}{L_{\text{linei}}} & \ldots & 0 & \frac{-1}{L_{\text{linei}}} & \ldots \end{bmatrix}_{2 \times (2m)} . \quad (61)$$

$$\frac{di_{\text{loadQi}}}{dt} = \frac{-R_{\text{loadi}}}{L_{\text{loadi}}} i_{\text{loadQi}} - \omega i_{\text{loadDi}} + \frac{1}{L_{\text{loadi}}} v_{bQi}. \quad (63)$$

Hence, for a network with p load points the small-signal state-space model of loads is given by

$$[\Delta \dot{i}_{\text{loadDQ}}] = A_{\text{load}}[\Delta i_{\text{loadDQ}}] + B_{1\text{LOAD}}[\Delta v_{bDQ}] + B_{2\text{LOAD}}\Delta\omega. \quad (64)$$

In (64)

$$[\Delta i_{\text{loadDQ}}] = [\Delta i_{\text{loadDQ 1}} \ \Delta i_{\text{loadDQ 2}} \ \cdots \ \Delta i_{\text{loadDQ }p}]^T \quad (65)$$

$$A_{\text{load}} = \begin{bmatrix} A_{\text{load 1}} & 0 & \cdots & 0 \\ 0 & A_{\text{load 2}} & \cdots & 0 \\ \cdots & \cdots & \cdots & \cdots \\ 0 & 0 & \cdots & A_{\text{load p}} \end{bmatrix}_{2p \times 2p} \quad (66)$$

$$B_{1\text{LOAD}} = \begin{bmatrix} B_{1\text{LOAD 1}} \\ B_{1\text{LOAD 2}} \\ .. \\ . \\ B_{1\text{LOAD p}} \end{bmatrix}_{2p \times (2m)}$$

$$B_{2\text{LOAD}} = \begin{bmatrix} B_{2\text{LOAD 1}} \\ B_{2\text{LOAD 2}} \\ .. \\ .. \\ B_{2\text{LOAD p}} \end{bmatrix}_{2p \times (1)} \quad (67)$$

where

$$A_{\text{loadi}} = \begin{bmatrix} \frac{-R_{\text{loadi}}}{L_{\text{loadi}}} & \omega_0 \\ -\omega_0 & \frac{-R_{\text{loadi}}}{L_{\text{loadi}}} \end{bmatrix} \quad B_{2\text{LOADi}} = \begin{bmatrix} I_{\text{loadQi}} \\ -I_{\text{loadDi}} \end{bmatrix}$$

$$B_{1\text{LOADi}} = \begin{bmatrix} \cdots & \frac{1}{L_{\text{loadi}}} & 0 & \cdots \\ \cdots & 0 & \frac{1}{L_{\text{loadi}}} & \cdots \end{bmatrix}_{2 \times (2m)}. \quad (68)$$

E. Complete Microgrid Model

It can be seen in (40), (55), and (64) that the node voltages are treated as inputs to each subsystem. To ensure the node voltage is well defined (and that the numerical solution well conditioned) a virtual resistor r_N is assumed between each node and ground. The resistance of virtual resistor is chosen sufficiently large such that its introduction would have minimum influence on the dynamic stability of the system. Hence, the voltage of ith node is given by

$$v_{bDi} = r_N(i_{oDi} - i_{\text{loadDi}} + i_{\text{lineD i,j}}) \quad (69)$$
$$v_{bQi} = r_N(i_{oQi} - i_{\text{loadQi}} + i_{\text{lineQ i,j}}). \quad (70)$$

In symbolic form, for a network with m nodes

$$[\Delta v_{bDQ}] = R_N (M_{\text{INV}}[\Delta i_{oDQ}] + M_{\text{load}}[\Delta i_{\text{loadDQ}}] + M_{\text{NET}}[\Delta i_{\text{lineDQ}}]). \quad (71)$$

In (71), matrix R_N is of size $2m \times 2m$, whose diagonal elements are equal to r_N. The mapping matrix M_{INV} is of size $2m \times 2s$, which maps the inverter connection points onto network nodes. For example, if ith inverter is connected at jth node, the element $M_{\text{INV}}(j, i)$ will be 1 and all the other elements in that row will be 0. Similarly, M_{load} is of size $2m \times 2p$ maps load connection points onto the network nodes with -1. Matrix M_{NET} of size $2m \times 2n$ maps the connecting lines onto the network nodes. Here care should be taken to put either $+1$ or -1 based on whether the given line current is entering or leaving the node.

Now, the complete microgrid small-signal state-space model and hence the system state matrix [as given in (72)] can be obtained by using the individual subsystem models given by (40), (41), (55), (64), and (71)

$$\begin{bmatrix} \Delta \dot{x}_{\text{INV}} \\ \Delta i_{\text{lineDQ}} \\ \Delta i_{\text{loadDQ}} \end{bmatrix} = A_{mg} \begin{bmatrix} \Delta x_{\text{INV}} \\ \Delta i_{\text{lineDQ}} \\ \Delta i_{\text{loadDQ}} \end{bmatrix}. \quad (72)$$

The complete system state matrix A_{mg} is given in (73). The small-signal flow among all the sub-modules is shown in Fig. 2 and (73), shown at the bottom of the page.

III. EIGENVALUE AND SENSITIVITY ANALYSIS

The eigenvalue concept of control theory has been extensively used to determine the stability of conventional power systems. Eigenvalues, termed modes, are the solution of the characteristic equation of a system's linearized state matrix [15]. Eigenvalues reveal the different frequency components in the system and their available damping.

A. Sensitivity Analysis

Further information on the origin of different frequency components can be obtained by observing the participation of different state variables in a particular mode [15]. This can be achieved with a sensitivity analysis conducted on the system state matrix. The sensitivity factor p_{ki}, given by (74), is the measure of the association between the state variables and the modes and is equal to the sensitivity of the eigenvalue λ_i to the diagonal element a_{kk} of the system state matrix. Sensitivity factors can be calculated using left and right eigenvectors

$$p_{ki} = \frac{\partial \lambda_i}{\partial a_{kk}}. \quad (74)$$

$$A_{mg} = \begin{bmatrix} A_{\text{INV}} + B_{\text{INV}} R_N M_{\text{INV}} C_{\text{INVc}} & B_{\text{INV}} R_N M_{\text{NET}} & B_{\text{INV}} R_N M_{\text{load}} \\ B_{1NET} R_N M_{\text{INV}} C_{\text{INVc}} + B_{2NET} C_{\text{INV}\omega} & A_{\text{NET}} + B_{1NET} R_N M_{\text{NET}} & B_{1NET} R_N M_{\text{load}} \\ B_{1\text{LOAD}} R_N M_{\text{INV}} C_{\text{INVc}} + B_{2\text{LOAD}} C_{\text{INV}\omega} & B_{1\text{LOAD}} R_N M_{\text{NET}} & A_{\text{load}} + B_{1\text{LOAD}} R_N M_{\text{load}} \end{bmatrix}. \quad (73)$$
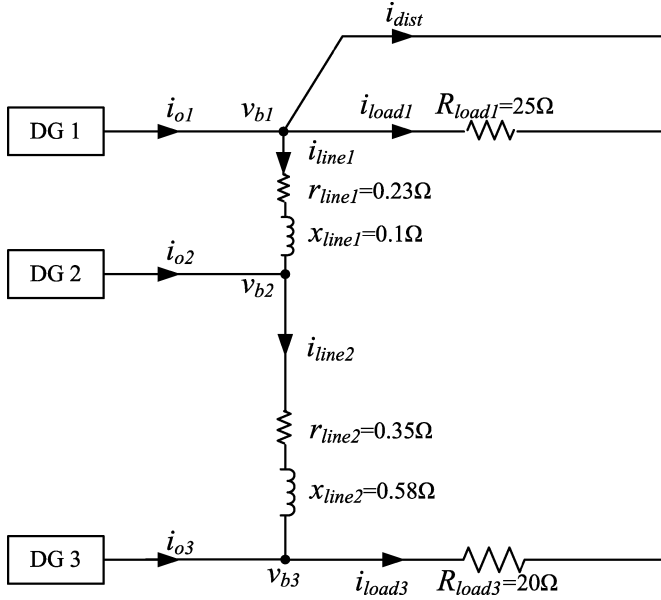
Fig. 10. Test system.

TABLE I
TEST SYSTEM PARAMETERS

Inverter parameters (10 kVA rating)			
Parameter	Value	Parameter	Value
f_s	8 kHz	m_p	9.4e-5
L_f	1.35 mH	n_q	1.3e-3
C_f	50 μF	K_{pv}	0.05
r_f	0.1 Ω	K_{iv}	390
L_c	0.35 mH	K_{pc}	10.5
r_{Lc}	0.03Ω	K_{ic}	16e3
ω_c	31.41	F	0.75
Network and Load parameters (see Fig. 10)			

TABLE II
INITIAL CONDITIONS

Par.	Value	Par.	Value
V_{od}	[380.8 381.8 380.4]	V_{oq}	[0 0 0]
I_{od}	[11.4 11.4 11.4]	I_{oq}	[0.4 -1.45 1.25]
I_{ld}	[11.4 11.4 11.4]	I_{lq}	[-5.5 -7.3 -4.6]
V_{bd}	[379.5 380.5 379]	V_{bq}	[-6 -6 -5]
ω_0	[314]	δ_0	[0 1.9e-3 -0.0113]
I_{line1d}	[-3.8]	I_{line1q}	[0.4]
I_{line2d}	[7.6]	I_{line2q}	[-1.3]

there can be various types of sources of DG and the droop gains and the sharing ratios may be dictated by the economic interest of the system operators. The choice of droop gains in such cases is further discussed in [16]. The objective of this paper is to investigate the stability of the system for the chosen values of droop gains. The model discussed in the previous section is general and it allows the users to investigate the system stability for any chosen combination of the system parameters.

In the design of the inverter output filter, the main criteria was to achieve attenuation by a factor of 100 in switching frequency ripple in the output voltage. This requires a resonant frequency of $10\times$ less than the switching frequency, which is a common rule of thumb. The filter inductor value was chosen to have low ripple content in the inductor current and, when combined with the capacitor value, gives the required resonant frequency. A large coupling inductance results in a poor bus voltage regulation. Hence, in this application the coupling inductance was chosen to provide a reasonable coupling impedance between the inverter output and the connection bus with a good bus voltage regulation.

The proportional and integral gains of the voltage controller, shown in Table I, were chosen using classical pole-zero and bode techniques to yield a bandwidth of 400 Hz for the voltage controller. The current feed-forward gain F was chosen to yield a low output impedance and hence improve the disturbance rejection of the inverter system. The current controller was designed for 1.6-kHz bandwidth with good rejection of high-frequency disturbance. Although, the control was implemented in the discrete-time domain, the equivalent continuous domain gains are provided (in Table I) for construction of the model.

A. Modeling Results

A complete model of the test system was obtained using the procedure outlined in Section II. Initial conditions of the system are given in Table II. These steady-state operating point conditions were obtained from a MATLAB/SIMULINK time-step simulation of the system. However, it is possible to use a more general load-flow solution as is often done in conventional power system modeling to obtain initial steady-state conditions [15]. The value chosen for virtual resistor (r_N) was 1000 Ω.

Fig. 11 shows the complete eigenvalues of the system for the initial conditions given in Table II. It can be seen that a large range of frequency components exist and that these fall in to three different clusters. Using (74), participation values of the

IV. EXPERIMENTAL VERIFICATION OF MODEL

A 220 V (per phase RMS), 50 Hz prototype microgrid was built to test and verify the model results. As shown in Fig. 10 the test system consist of three inverters of equal rating (10 kVA) with two load banks, one at each bus 1 and bus 3. These inverters are controlled to share the real and reactive powers over the lines 1 and 2. System parameters are given in Table I. Network is resistance dominated as is the case in low voltage distribution systems. DG1 and DG2 are located relatively close together compared to DG3. In this test system only resistive loads were used to verify the model. A resistive load of 5.8 kW (= 25 Ω per phase) at bus 1 and 7.3 kW (= 20 Ω per phase) at bus 2 is considered as an initial operating point.

In the test system analyzed in this paper all the inverters are equally rated. Hence, the droop gains of all the inverters were chosen to be equal so that they equally share the fundamental power. The nominal frequency droop was 0.3% at the maximum real power output, whereas the nominal voltage droop was 2% at the maximum reactive power output. In a practical scenario
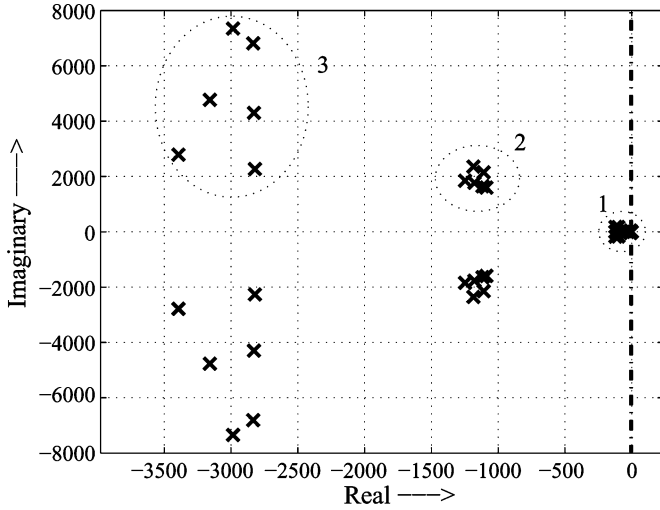
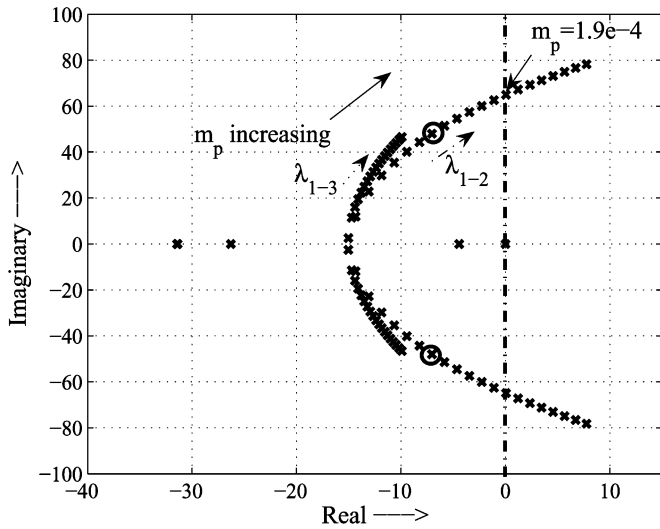Fig. 11.   Eigenvalue spectrum of the system indicating various modes.

Fig. 12.   Trace of low-frequency modes as a function of real power droop gain: $1.57e^{-5}$ (0.05% droop) $\leq m_p \leq 3.14e^{-4}$ (1% droop).

TABLE III
SENSITIVITY OF LOW FREQUENCY DOMINANT MODES

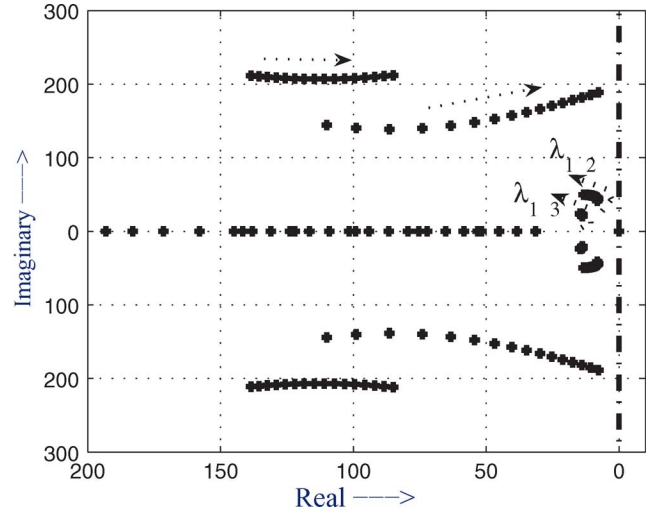| Sensitivity of λ_{1-2}		Sensitivity of λ_{1-3}	
state	participation	state	participation
P_1	0.15	P_1	0.12
Q_1	0.05	Q_1	0.06
P_2	0.3	P_3	0.32
Q_2	0.03	Q_3	0.03
δ_2	0.5	δ_3	0.57
remaining states ≤ 0.005			

Fig. 13.   Trace of low-frequency modes as function of reactive power droop gain: $3.17e^{-4}$ (0.5% droop) $\leq n_q \leq 4.8e^{-3}$ (8% droop).

different states in these eigenvalues can be obtained. This analysis shows that the high frequency modes in cluster "3" are sensitive to the state variables of LCL filter block of inverters and the line currents. The modes in cluster "2" are largely sensitive to the state variables of voltage controller, current controller, and output LC filter. The low frequency dominant modes shown in cluster "1" are largely sensitive to the state variables of the power controller.

Fig. 12 shows the trajectory of the two-pairs of complex-conjugate dominant low frequency eigenvalues (part of cluster 1) as a function of the real power droop gain m_p (the same value used for all the three inverters). The eigenvalues marked with λ_{1-2} are largely sensitive to the state variables of real power part of the power controllers of inverters 1 and 2, as given in Table III. Similarly, eigenvalue marked as λ_{1-3} are highly sensitive to the state variables of real power part of the power controllers of inverters 1 and 3. It is therefore apparent that the modes λ_{1-2} and λ_{1-3} represent the dynamics of real power sharing of the DGs. However, these modes are also sensitive to the reactive power.

This is a consequence of the coupling of real and reactive powers in the network due to the presence of highly resistive lines.

Fig. 12 shows that as m_p is increased, modes λ_{1-2} and λ_{1-3} move towards unstable region making the system more oscillatory and eventually leading to instability. It is to be noted that large droop gain is necessary to improve the transient response of DGs, whereas a low-pass filter with low cut-off frequency is needed to achieve good attenuation of high frequency distortion components in the measured power and to avoid any interaction with inner current controllers. Also, from Table III it can be observed that the dominant mode λ_{1-2} is highly sensitive to the states of the power controller of inverter 2. Hence, in this system, inverter 2 is the most critical element from the point of view of system stability. However, the low frequency dominant modes are less sensitive to the reactive power droop gain compared to the active power droop gain, as shown in Fig. 13.

B. Experimental Results

In this section results obtained from the model are verified against experimental testing using the system described at the beginning of Section IV. First, to verify the low frequency modes within the model, a disturbance in load current $i_{\text{load 1}}$ was arranged. This requires the addition of a controlled current source in parallel to R_{load1} shown in Fig. 10 and the addition of a disturbance term to (72). The disturbance was chosen to be
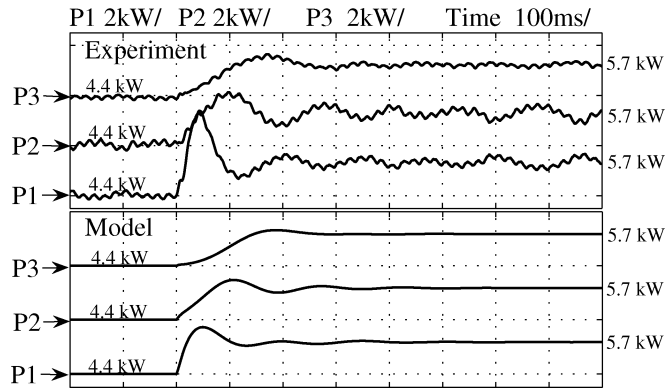
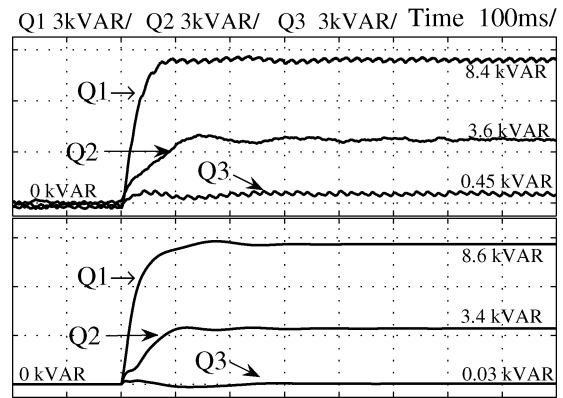Fig. 14. Active power (filtered) response of micro-sources with 3.8 kW of step change in load power at bus 1.

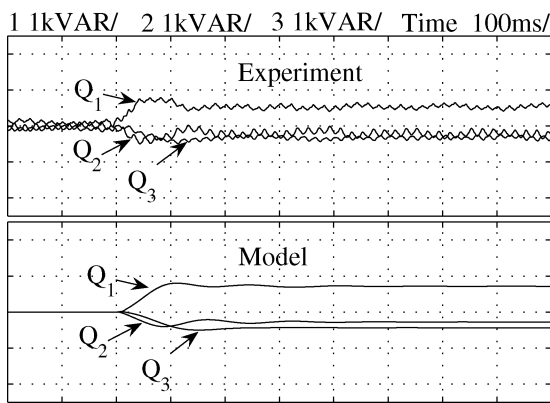

Fig. 15. Reactive power exchange between the micro sources with 3.8 kW of step change in load power at bus 1 (Initial values: $Q1 = 0$, $Q2 = -200$, $Q3 = +200$; Final values: $Q1 = +600$, $Q2 = -300$, $Q3 = -200$).

Fig. 16. Active power (filtered) response of micro-sources with 16.8 kW and 12 kVAR RL load step change at bus 1.
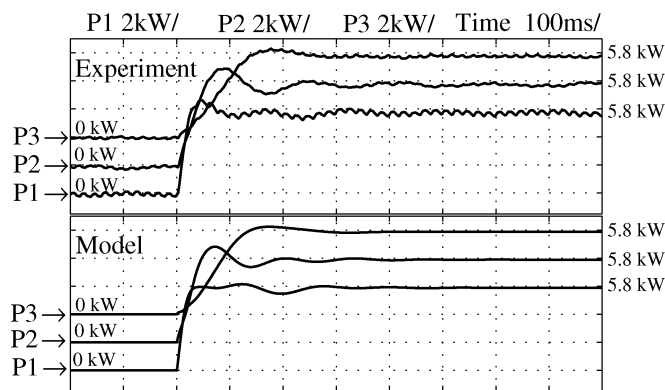

Fig. 17. Reactive power (filtered) response of micro-sources with 16.8 kW and 12 kVAR RL load step change at bus 1.
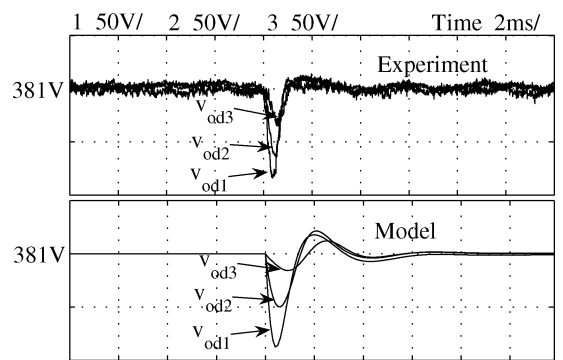

Fig. 18. Output voltage (d-axis) response with 27 kW of step change in load power at bus 1.
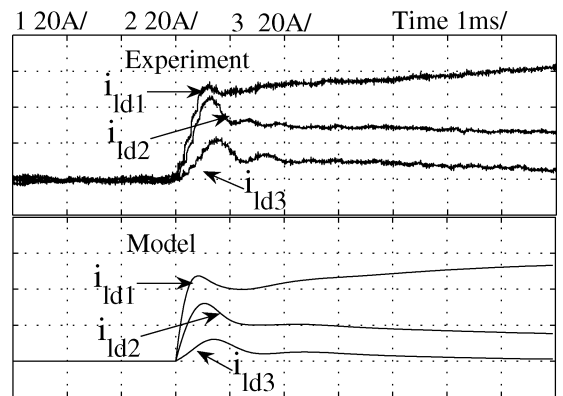

Fig. 19. Inductor current (d-axis) response with 27 kW of step change in load power at bus 1.

a step change of 3.8-kW real power. The experimental system was excited with the same 3.8-kW step change in load at bus 1. A second set of tests was used to examine the low frequency modes under a severe step change in RL load connected at bus 1. A third test was used to examine the high frequency modes. Due to the presence of significant damping, a large disturbance in the load was needed to capture the high frequency modes. A step change of 27 kW (from no load) at bus 1 was considered.

Figs. 14–19 shows the response of state variables P, Q, v_{od} and i_{ld} of all the three inverters obtained from the model and

experiment. It is to be noted that the waveforms corresponding to the experimental results are actually the internal variables of inverters that were captured by using on-board D/A converters. Also, all these figures depict only the variation in the signal from their initial point (relative change).

Fig. 14, shows the DG fundamental output power response for a 3.8-kW step change in load 1, for both the model and experimental system. The dominant, poorly damped low frequency modes λ_{1-2} (marked with a circle in Fig. 12) of frequency 7.2 Hz can be clearly observed in the fundamental power. Although, a slight difference in the magnitude exists, the response obtained from the model matches with the response obtained

from the practical test system. Due to a slight unequal dc off-set in the measured output phase currents a small 50-Hz component was observed in the output power in the experimental case.

In Fig. 14 it can be seen that DG1, which is nearest to the changed load, took the major part of the transient whereas DG2 and DG3 have responded more slowly, depending on the effective impedance seen from the load point. Hence, during large changes in the load, closely located DGs may be overloaded and can be tripped out due to the limited overload capacity of the inverters.

Fig. 15 shows the fundamental reactive power sharing. It can be seen that a considerable amount of reactive power was exchanged between the inverters even though the step was in the real power. This was because of the presence of significant resistance in the lines. This effect can be reduced by increasing the voltage magnitude droop but this will be at the expense of voltage quality. This is one of the major limitations of conventional droop control applied in low voltage grids [17], [18]. Again, it can be observed that the experimental results closely match the model results.

To investigate the low frequency mode response under severe test load conditions, a test involving a step change of an RL load was conducted. In this test, there was initially no load connected to the system and then a load of 16.8 kW and 12 kVAR at bus 1 was switched on. Figs. 16 and 17 show the active and reactive power response of the inverters under such load transient. In both cases the results from the model closely match the experimental results. This indicates that the dominant low-frequency modes are not particularly dependant on the system load level. Also, it can be inferred that the reactive power sharing is rather poor in this case. However, this can be improved by increasing the reactive power droop gains but at the expense of poor bus voltage regulation.

Fig. 18 depicts the output voltage response of all the three inverters for a 27-kW load change. The high frequency modes of frequency around 350 Hz in cluster "2" shown in Fig. 11 can be observed in the output voltage response. A notch of 20% for less than 1 ms can be seen in the output voltage of inverter 1 which is closer to the load point. Although, a slight difference exists in the magnitude of response obtained from the linear model compared to the test system, the oscillatory response in both cases matches. Also, the response obtained from the experimental set-up is more damped than that of the model. It is to be noted that the output voltage state variable has the maximum participation in these modes. It would be interesting to investigate the possible excitation of these modes under harmonic loads because the lower order significant harmonic frequencies will fall in the range of frequencies of these modes.

Fig. 19 shows the inductor current response of all the three inverters. In this case, high frequency modes with a frequency of around 800 Hz in cluster "3" in Fig. 11 can be observed in the response. It was observed that these modes are highly sensitive to the system load level which determines their damping.

V. CONCLUSION

In this paper, a small-signal state-space model of a microgrid is presented. The model includes inverter low frequency dynamics, high frequency dynamics, network dynamics, and load dynamics. All the sub-modules are individually modeled and are then combined on a common reference frame to obtain the complete model of the microgrid.

The model was analyzed in terms of the system eigenvalues and their sensitivity to different states. With the help of this analysis the relation between different modes and system parameters was established. It was observed that the dominant low-frequency modes are highly sensitive to the network configuration and the parameters of the power sharing controller of the micro sources. The high frequency modes are largely sensitive to the inverter inner loop controllers, network dynamics, and load dynamics.
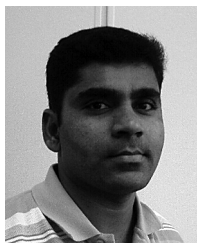
Results obtained from the model were verified experimentally on a prototype microgrid. It was observed that the model successfully predicts the complete microgrid dynamics both in the low and high frequency range.

Small signal modeling has had a long history of use in conventional power systems. The inverter models (and the inclusion of network dynamics) illustrated in this paper allow microgrids to be designed to achieve the stability margin required of reliable power systems.

REFERENCES

[1] R. H. Lasseter, "Microgrids," in *Proc. Power Eng. Soc. Winter Meeting*, Jan. 2002, vol. 1, pp. 305–308.

[2] A. Arulapalam, M. Barnes, A. Engler, A. Goodwin, and N. Jenkins, "Control of power electronic interfaces in distributed generation microgrids," *Int. J. Electron.*, vol. 91, no. 9, pp. 503–523, Sep. 2004.

[3] R. Lassetter, "Integration of Distributed Energy Resources: The CERTS Microgrid Concept," CERT Rep., Apr. 2002.

[4] M. S. Illindala, P. Piagi, H. Zhang, G. Venkataramanan, and R. H. Lasseter, "Hardware Development of a Laboratory-Scale Microgrid Phase 2: Operation and Control of a Two-Inverter Microgrid," Nat. Renewable Energy Rep., Mar. 2004.

[5] Y. Li, D. M. Vilathgamuwa, and P. C. Loh, "Design, analysis and real-time testing of a controller for multibus microgrid system," *IEEE Trans. Power Electron.*, vol. 19, no. 5, pp. 1195–1204, Sep. 2004.

[6] E. A. A. Coelho, P. Cortizo, and P. F. D. Gracia, "Small signal stability for parallel-connected inverters in stand-alone ac supply systems," *IEEE Trans. Ind. Appl.*, vol. 38, no. 2, pp. 533–542, Mar./Apr. 2002.

[7] J. M. Guerrero, L. G. V. Na, M. Castilla, and J. Miret, "A wireless controller to enhance dynamic performance of parallel inverters in distributed generation systems," *IEEE Trans. Power Electron.*, vol. 19, no. 5, pp. 1205–1213, Sep. 2004.

[8] A. L. Dimeas and N. D. Hatziargyriou, "Operation of a multiagent system for microgrid control," *IEEE Trans. Power Syst.*, vol. 20, no. 3, pp. 1447–1455, Aug. 2005.

[9] M. Prodanović, T. Green, and H. Mansir, "A survey of control methods for parallel three-phase inverters connection," *Proc. Inst. Elect. Eng.*, no. 475, pp. 472–477, Sep. 2000.

[10] M. C. Chandorker, D. M. Divan, and A. Rambabu, "Control of parallel connected inverters in stand-alone ac supply systems," *IEEE Trans. Ind. Appl.*, vol. 29, no. 1, pp. 136–143, Jan./Feb. 1993.

[11] J. M. Undrill, "Dynamic stability calculations for an arbitrary number of interconnected synchronous machines," *IEEE Trans. Power Apparat. Syst.*, vol. PAS-87, no. 3, pp. 835–845, Mar. 1968.

[12] M. N. Marwali, J. Jung, and A. Keyhani, "Control of distributed generation systems—part II: load sharing control," *IEEE Trans. Power Electron.*, vol. 19, no. 6, pp. 1551–1561, Nov. 2004.

[13] M. Prodanović, "Power Quality and Control Aspects of Parallel Connected Inverters in Distributed Generation," Ph.D. dissertation, Imperial College, Univ. London, London, UK, 2004.

[14] M. N. Marwali and A. Keyhani, "Control of distributed generation systems—Part I: voltages and current control," *IEEE Trans. Power Electron.*, vol. 19, no. 6, pp. 1541–1550, Nov. 2004.

[15] P. Kundur, *Power System Stability and Control*. New York: McGraw-Hill, 1994.

[16] C. A. Hernandez-Aramburo, T. C. Green, and N. Mugniot, "Fuel consumption minimization of a microgrid," *IEEE Trans. Ind. Appl.*, vol. 41, no. 3, pp. 673–681, May/Jun. 2005.

[17] A. Tuladhar, H. Jin, T. Unger, and K. Mauch, "Control of parallel inverters in distributed ac power systems with consideration of line impedance effect," *IEEE Trans. Ind. Appl.*, vol. 36, no. 1, pp. 131–138, Jan./Feb. 2000.

[18] A. Engler, "Applicability of droops in low voltage grids," *Int. J. Distrib. Res.*, vol. 1, no. 1, pp. 3–15, Sep. 2004.

Milan Prodanović (M'01) received the B.Sc. degree in electrical engineering from the University of Belgrade, Belgrade, Serbia, in 1996 and the Ph.D. degree from Imperial College, London, U.K., in 2004.

He is currently a Research Associate at Imperial College. From 1997 to 1999, he was engaged with GVS Engineering Company, Serbia, developing power electronic circuits and control algorithms for inverter and UPS systems. His research interests are in digital control of power electronic systems, computer-aided analysis and design of power converters, power quality, micro-grids, and distributed generation.

Nagaraju Pogaku (S'04) received the B.Eng. degree in electrical and electronics engineering from Osmania University, Hyderabad, India, in 2000, the M.Tech. degree in electrical engineering (with a specialization in power electronics and power systems) from the Indian Institute of Technology, Bombay, in 2003, and is currently pursuing the Ph.D. degree in the Department of Electrical and Electronics Engineering, Imperial College, London, U.K.

His research interests include distributed generation, microgrids, application of power electronics to power systems, and power system deregulation.

Timothy C. Green (M'89–SM'02) received the B.Sc. degree (first class honours) in electrical engineering from Imperial College, London, U.K., in 1986 and the Ph.D. degree in electrical engineering from Heriot-Watt University, Edinburgh, U.K., in 1990.

He was a Lecturer at Heriot Watt University until 1994 and is now a Professor of Electrical Power Engineering at Imperial College London and Deputy Head of the Control and Power Research Group. His research interest is in using power electronics and control to enhance power quality and power delivery. This covers interfaces and controllers for distributed generation, micro-grids, active distribution networks, FACTS and active power filters. He has an additional line of research in power MEMS and energy scavenging.

Dr. Green is a Chartered Engineer in the U.K. and MIEE.